

# NONUNIFORMITY OF HYBRID ADSORBENTS

V.M. Gun'ko<sup>1</sup>, R. Leboda<sup>2</sup>, V.V. Turov<sup>1</sup>, and F. Villieras<sup>3</sup>

<sup>1</sup>*Institute of Surface Chemistry, 17 General Naumov Street, 03164 Kyiv, UKRAINE*

<sup>2</sup>*Department of Chemical Physics, M. Curie-Sklodowska University, 20031 Lublin, POLAND*

<sup>3</sup>*Laboratoire Environnement et Mineralurgie, INPL et CNRS UNR 7569, ENSG, BP40, 54501 Vandoeuvre les Nancy cedex, FRANCE*

## Abstract

Several series of pyrocarbon-mineral adsorbents (carbosils) were studied using the nitrogen adsorption method to compute structural and energetic parameters within the scope of overall adsorption isotherm approximation applying regularization procedure with consideration for surface heterogeneity. A portion of pyrocarbon deposits (graphene clusters) fills mesopores of the oxide supports, but another portion represents relatively large nonporous pyrocarbon globules formed on the outer surfaces of the oxide matrices. Contributions of these two types of pyrocarbon deposits depend on the nature of oxide matrices and carbonized precursors.

## Introduction

Textural characteristics of hybrid pyrocarbon-mineral adsorbents depend on features of both oxide matrices and organic precursors as well as on pyrolysis conditions [1-7]. Clearly, the pyrocarbon structure can significantly differ from that of an oxide support; therefore application of standard adsorption isotherm equations to such hybrid adsorbents gives average characteristics with marked errors due to neglect of the mentioned heterogeneity. For instance, pores of carbon deposits can be partially slitlike (micropores), cylindrical (mesopores) or correspond to gaps between dense nonporous spherical particles, but pores of oxide matrices can be of other shape, e.g., relatively smooth cylindrical mesopores in silica gel particles. Many of adsorption equations include some parameters dependent of the pore shape [8-11]; therefore the pore size distribution (PSD)  $f(R_p)$  determined for complex adsorbents using one of such equations can be inadequate for one of the adsorbent components (if the method depends on the pore shape). Additionally, some equations can be applied to mesoporous adsorbents, but others are used only for microporous ones. However, complex adsorbents typically possess broadened PSDs including pores of different shapes. Therefore, many of adsorption isotherm equations are utilized for restricted pressure ranges, which correspond to filling of pores of one of types, and corrected isotherms are used to determine the parameters for other pores (e.g., consideration for adsorption in mesopores to calculate the parameters of micropores) [8-12]. However, such an approach can introduce additional poorly controlled errors in the determined structural parameters. Besides, the relationship between the PSD and the adsorption energy distribution  $f(E)$  is ambiguous for hybrid adsorbents, as  $f(E)$  depends not only on the pore structure but also on the nature of the adsorbent surfaces, that restricts the application of the corresponding equations to compute  $f(R_p)$  if the corresponding equations include energetic parameters instead of structural ones. Additionally, neglect of the heterogeneity of complex adsorbents determining  $f(E)$  can lead to the distortion of the  $f(E)$  shape, as the equation constants can depend on the surface nature [8-11] and the  $f(E)$  distributions for components of hybrid materials can be different. Clearly, the application of the adsorption isotherm equations independent of the adsorbent nature (e.g.,

Fowler-Guggenheim or deBoer-Hill equations) for computations of the overall  $f(E)$  does not give information about the  $f(E)$  dependence on the textural and chemical properties of adsorbent components in details. Therefore, the aim of this work is consideration for the heterogeneity of hybrid carbon-mineral adsorbents in details on the study of the structural and energetic characteristics on the basis of adsorption-desorption data.

## Experimental

(a) *Materials.* Silica gel Si-60 (Schuchardt München, Germany) was used to prepare pyrocarbon-silica gel samples by pyrolysis of  $\text{CH}_2\text{Cl}_2$  in a stainless steel autoclave (0.3 L) at 823K for 0.5, 1, 2, 3, 4, and 6 h corresponding to different CS-*i* carbosils with various amounts of pyrocarbon  $C_c$  (Table 1) [6,7]. Acenaphthene  $\text{C}_{12}\text{H}_{10}$  (0.5, 2 or 3 g per 5 g of silica gel corresponding to AN1, AN2, and AN3 samples at  $C_c = 7.0, 15.8, \text{ and } 22.7$  wt.% respectively) carbonized on silica gel Si-60 (Merck) in the autoclave at 773K for 6 h. Acetylacetone  $\text{C}_5\text{H}_8\text{O}_2$  (L. Light Co.) in the amounts of 0.02, 0.03 and 0.04 M pyrolyzed on 5 g of Si-60 (Merck) at 773K for 6 h gave the series of carbosils AC1, AC2 and AC3. Glucose  $\text{C}_6\text{H}_{12}\text{O}_6$  of 6 g pyrolyzed on 10 g of Si-60 (Merck) under the same conditions gave carbosil Gl. Hydrothermal treatment of Si-60 (Merck) (labeled HTT) was carried out in the autoclave (0.3 L) containing 20 mL of water at 423K for 6 h using 2 g of silica gel or carbosil placed in a quartz vessel [14].

**Table 1**  
Structural Parameters of S-60 Initial and Hydrothermally Treated (HTT) at 423K, and Different Carbosils

Sample	$C_c$ , wt. %	$S_{BET}$ , $\text{m}^2/\text{g}$	$V_g$ , $\text{cm}^3/\text{g}$	$r_p$ , nm
Si-60 (Merck)		369	0.753	4.1
Si-60HTT		121	0.731	12.1
AN1/Si-60	7	327	0.650	4.8
AN2/Si-60	15.8	244	0.480	3.9
AN3/Si-60	22.7	233	0.453	3.9
AC1	4	339	0.717	4.2
AC2	9.1	296	0.606	4.1
AC3	14.5	275	0.566	4.1
Gl	16.5	174	0.433	5.0
Si-60 (Schuchardt München)		372	0.800	4.3
CS-1	0.8	366	0.74	4.0
CS-2	4.4	339	0.67	4.0
CS-3	14.9	299	0.56	3.8
CS-4	20.3	259	0.47	3.6
CS-5	26.7	223	0.39	3.5
CS-6	35.0	163	0.28	3.4

Additionally, Si-60 (Merck) was utilized to prepare carbon/X/silica materials (carbosils  $\text{CS}_X$ ) by pyrolysis of such metal acetylacetonates (AcAc) as  $\text{Zr}(\text{AcAc})_4$ ,  $\text{TiO}(\text{AcAc})_2$ ,  $\text{Ni}(\text{AcAc})_2$ ,  $\text{Zn}(\text{AcAc})_2$ ,  $\text{Cr}(\text{AcAc})_3$  and  $\text{Co}(\text{AcAc})_2$  (Aldrich) in the autoclave at

773K for 6 h. The utilization of the same amounts (0.01 M) of metal acetylacetonates results in deposition of equal amounts of metal moles but different amounts of moles of acetylacetonate groups, as the  $n$  values in  $M(\text{AcAc})_n$  compounds are different ( $n = 2-4$ ). These carbon-mineral adsorbents were labeled as  $\text{CS}_{\text{Ti}}$ ,  $\text{CS}_{\text{Cr-1}}$ ,  $\text{CS}_{\text{Co}}$ ,  $\text{CS}_{\text{Ni}}$ ,  $\text{CS}_{\text{Zn}}$ , and  $\text{CS}_{\text{Zr-1}}$ . The metal valence in  $M(\text{AcAc})_n$  was taken into consideration and  $2/3 \times 0.01$  M of chromium acetylacetonate ( $\text{CS}_{\text{Cr-2}}$ ) and  $2/4 \times 0.01$  M of zirconium acetylacetonate ( $\text{CS}_{\text{Zr-2}}$ ) were utilized (Table 2) [4]. Concentrations of X phases (grafted metal compounds,  $C_X$ ) and pyrocarbon ( $C_C$ ) are shown in Table 2. Silica gel Si-40 (Merck) was used to prepare pyrocarbon-silica by pyrolysis of acenaphthene (0.5, 1, 2 or 3 g per 5 g of silica gel corresponding to  $\text{Ani/Si-40}$ ,  $i = 1-4$ , at  $C_C = 5.6, 8.3, 19.2$ , and  $21.8$  wt.% respectively) carbonized in the autoclave at 773K for 6 h (Table 3) [15]. Hydrothermal treatment of Si-40 (labeled HTT) was carried out in the autoclave at 423K for 6 h similarly to that for Si-60. Mesoporous silica gel KSK-2 (Russia) was utilized to prepare titania-silica gel (CVD-TSG) adsorbents by means of the chemical vapor deposition (CVD) technique [16] for  $\text{TiCl}_4$  chemisorbed and hydrolyzed at 473K (K28) and 873K (K68, Table 4) using eight cycles of the chemisorption-hydrolysis. Carbon-oxide samples were synthesized using pyrolysis of cyclohexene at the silica gel (K03) and CVD-TSG (K282, K682) surfaces at a constant partial pressure 51.3 mm Hg in a flow reactor under isothermal conditions and gravimetric control at 973K for 5 h (Table 4) [2,17].

**Table 2**  
Concentrations of Metal Compounds and Grafted Carbon in CS Samples (Si-60)

Sample	X phase	$C_X$ , wt%	$C_C$ , wt.%	$S_{\text{BET}}$ , $\text{m}^2/\text{g}$	$V_p$ , $\text{cm}^3/\text{g}$	$r_p$ , nm
$\text{CS}_{\text{Ti}}$	$\text{TiO}_2$ (anatase)	11.37	9.2	192	0.419	4.35
$\text{CS}_{\text{Cr-1}}$	$\text{Cr}_2\text{O}_3$ (amorph.)	11.26	12.0	278	0.443	3.19
$\text{CS}_{\text{Cr-2}}$	$\text{Cr}_2\text{O}_3$ (amorph.)	8.28	4.8	293	0.622	4.24
$\text{CS}_{\text{Co}}$	Co	8.42	6.1	187	0.524	5.56
$\text{CS}_{\text{Ni}}$	Ni, NiO	9.42	5.9	263	0.566	4.27
$\text{CS}_{\text{Zn}}$	$\text{Zn}_2\text{SiO}_4$	10.98	6.5	212	0.536	5.05
$\text{CS}_{\text{Zr-1}}$	$\text{ZrO}_2$	17.14	13.8	236	0.415	3.52
$\text{CS}_{\text{Zr-2}}$	$\text{ZrO}_2$	10.19	7.4	281	0.537	3.82

**Table 3**  
Structural Parameters of Si-40 Initial and After Hydrothermal Treatment (HTT) at 423K, Carbons ANi Prepared by Pyrolysis of Acenaphthene

Sample	$C_C$ , wt.%	$S_{\text{BET}}$ , $\text{m}^2/\text{g}$	$V_p$ , $\text{cm}^3/\text{g}$	$r_p$ , nm
Si-40	-	732	0.542	1.48
Si-40HTT	-	309	0.512	3.31
AN1/Si-40	5.6	313	0.375	2.40
AN2/Si-40	8.3	231	0.317	2.74
AN3/Si-40	19.2	128	0.163	2.53
AN4/Si-40	21.8	92	0.149	3.24

C/A-300 samples (Table 5) were synthesized by the pyrolysis of  $\text{CH}_2\text{Cl}_2$  at the fumed silica substrate (A-300 with the specific surface area  $S_{\text{BET}} \approx 300 \text{ m}^2 \text{ g}^{-1}$ ) at 673-823K for 40-120 min. The technique of sample preparation was described in detail elsewhere [3]. Other carbosil samples with the highly disperse oxide matrices were synthesized using the pyrolysis of cyclohexene at 973 K for 240 min (Table 5) [2]. Fumed silica, alumina, titania, and mixed X/SiO<sub>2</sub> (X = Al<sub>2</sub>O<sub>3</sub> (AS), TiO<sub>2</sub> (TS), Al<sub>2</sub>O<sub>3</sub>/TiO<sub>2</sub> (AST)) (Pilot Plant of the Institute of Surface Chemistry, Kalush, Ukraine) and C/X/SiO<sub>2</sub> were studied at different concentrations ( $C_X$ ) of X oxide phase (Table 5) [18,19a].

**Table 4**  
Structural Parameters of Silica gel KSK, CVD-TiO<sub>2</sub>/KSK (K28, K68) and After Carbonization of Cyclohexene (K03, K282, K682)

Sample	$C_{\text{TiO}_2}$ , wt%	$C_C$ , wt%	$S_{\text{BET}}$ , $\text{m}^2/\text{g}$	$V_p$ , $\text{Cm}^3/\text{g}$	$r_p$ , nm
KSK			377	0.98	5.2
K28	24.4	-	228	0.54	4.8
K68	17.9	-	281	0.76	5.4
K03		20.5	289	0.66	4.8
K282		20.5	152	0.31	4.0
K682		19.9	204	0.49	4.8

(b) *Nitrogen adsorption.* Nitrogen adsorption-desorption isotherms were recorded at 77.4K using a Micromeritics ASAP 2010 adsorption analyzer at  $p/p_0 > 10^{-3}$ - $10^{-4}$ , where  $p$  and  $p_0$  denote the equilibrium pressure and the saturation pressure of nitrogen at 77.4K, respectively. Additionally, the low-pressure adsorption isotherms were obtained for some samples (CS-i, Table 1) at  $10^{-8} < p/p_0 < 0.15$  using a technique described elsewhere [7,21]. The specific surface area  $S_{\text{BET}}$  was calculated using standard BET method. The pore volume  $V_p$  was determined from adsorption at  $p/p_0 \approx 0.98$ - $0.99$ . Average value of pore radius  $r_p$  was estimated as follows  $r_p = 2V_p/S_{\text{BET}}$ . The isotherms for unmodified or modified mesoporous silica gels (such as Si-60, Si-40 and KSK) correspond to the IV type [8,9] with marked hysteresis loops. The isotherms for fumed oxides are close to the II type but have narrow hysteresis loops at  $p/p_0 > 0.75$  [3]. In this paper, the nitrogen adsorption-desorption isotherms are not shown (see Ref. [2-7]) while the corresponding  $\alpha_s$  plots are analyzed. To characterize the adsorptive properties of carbosils CS-i, the adsorption potential distributions  $f(A) = -da/dA$  (where  $a$  denotes the adsorbed amount of nitrogen;  $A = -\Delta G = R_g T \ln(p_0/p)$  is the differential molar work,  $R_g$  is the gas constant) can be also utilized.

(c) *Computing.* To consider the heterogeneity of hybrid adsorbents [22], the computational technique can be following: (a) calculations of the parameters ( $\lambda_{ij}$ ) of the adsorption isotherm equations  $a_j = \Theta_j(p, T, \lambda_{ij})$  (where  $T$  is the temperature,  $j$  is a number of an adsorbent component,  $i$  is a parameter number) using adsorption data for individual (synthesized under the same conditions that the corresponding phases in multi-component adsorbents) and complex materials with consideration for their features using direct minimization methods; (b) computing of the distribution functions  $f(x_n)$  of parameters  $x_n$  (e.g., pore radius  $R_p$ , adsorption energy  $E$ ) for complex adsorbents utilizing the sum

$$a = \sum_j c_j \Theta_j(p, T, \lambda_{ij}, x_n) \quad (1)$$

as the kernel of the overall adsorption isotherm equation

$$\theta(T, p) = \int_0^{x_{\max}} \sum_j c_j \Theta_j(T, p, \lambda_{ij}, x) f(x) dx \quad (2)$$

whose solution in respect to  $f(x)$  can be obtained with the regularization procedure [23,24]. The solution of Eq. (2) is known to be an ill-posed problem due to a marked influence of noise components on the experimental data (small changes in  $\theta(T, p)$  can result in large changes in  $f(x)$ , and there are many solutions of this equation fitting the experimental data), which do not allow one to use exact inversion formulas or iterative algorithms [11,23].

**Table 5**  
Structural Parameters of Fumed Silica, AS, TS and AST Before and After Carbonization

Sample	$C_X$ , wt%	$C_C$ , wt%	$S_{BET}$ , $m^2/g$	$V_p$ , $cm^3/g$	$r_p$ , nm
A-300		-	312	0.65	4.2
C/A-300 <sup>a</sup>		8.5	385	0.96	4.9
C/A-300 <sup>b</sup>		0.5	297	0.60	3.3
C/A-300 <sup>b</sup>		4	280	0.51	3.7
C/A-300 <sup>b</sup>		6.5	260	0.50	3.9
C/A-300 <sup>b</sup>		20	231	0.43	3.7
C/A-300 <sup>b</sup>		40	160	0.36	4.4
C/A-300 <sup>b</sup>		64	112	0.19	3.4
AS <sub>1</sub>	1.3	-	207	0.42	4.1
AS <sub>3</sub>	3	-	188	0.39	4.1
AS <sub>23</sub>	23	-	353	0.80	4.5
AS <sub>30</sub>	30	-	239	0.57	4.8
Al <sub>2</sub> O <sub>3</sub>			159	0.42	5.3
TiO <sub>2</sub>			60	0.17	5.7
AST	72	-	38	0.07	3.7
TS <sub>2</sub>	1.7 <sup>c</sup>	-	318	0.71	4.1
C/TS <sub>2</sub>		20.1	286	0.77	4.6
TS <sub>5</sub>	5 <sup>c</sup>	-	310	0.71	4.1
C/TS <sub>5</sub>		20.0	273	0.74	4.7
TS <sub>33</sub>	33 <sup>c</sup>	-	219	0.55	5.0
C/TS <sub>33</sub>		23.1	169	0.47	5.6
TS <sub>9</sub>	9 <sup>f</sup>	-	238	0.57	4.8
C/TS <sub>9</sub>		26.3	188	0.43	4.1
TS <sub>14</sub>	14 <sup>f</sup>	-	217	0.49	4.5
TS <sub>20</sub>	20 <sup>f</sup>	-	65	0.13	4.0
TS <sub>29</sub>	29 <sup>f</sup>	-	73	0.17	4.7
TS <sub>36</sub>	36 <sup>f</sup>	-	115	0.25	4.3
C/TS <sub>36</sub>		29.7	84	0.22	5.2

Note. Pyrolysis of <sup>a</sup>C<sub>6</sub>H<sub>10</sub> and <sup>b</sup>CH<sub>2</sub>Cl<sub>2</sub>; <sup>c</sup>CVD-TiO<sub>2</sub>/fumed silica; <sup>f</sup>fumed TS;  
X = Al<sub>2</sub>O<sub>3</sub>, TiO<sub>2</sub>, Al<sub>2</sub>O<sub>3</sub>/TiO<sub>2</sub>

The constants determined using direct minimization methods for local equations (2) depend on the nature of  $j$ -phase. The weighting coefficients  $c_j$  determine the accessibility of  $j$ -phase (which can differ from its concentration in a complex adsorbent) for adsorbate. For example, a grafted phase can easily block pores of support particles possessing relatively low external surfaces; and the narrower the pores, the larger the reduction of the pore volume due to pyrocarbon grafting on silica gels (Fig. 1). The  $c_j$  values can be estimated using different adsorbates, which adsorb predominantly onto one of the phases of hybrid adsorbents [1,7]. Additionally, the accessibility of the oxide surfaces of carbon-oxides adsorbents can be computed from the intensity (optical density) of the IR bands of free surface hydroxyls [3,25,26].

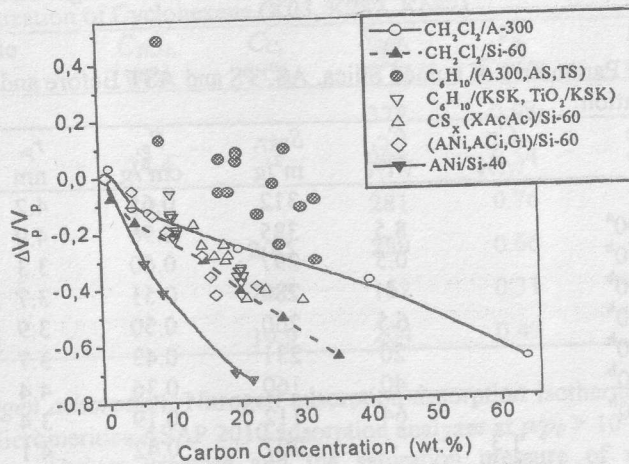


Fig. 1. Relative changes in the pore volume for carbosils due to grafting of pyrocarbon (precursors are shown) on different silicas.

The pore size distribution  $f(R_p)$  can be calculated using the overall adsorption isotherm equation [27], which can be written for  $j$ -phase as follows

$$a_j = \int_{r_{\min}(p)}^{r_k(p)} f(R_p) dR_p + \int_{r_k(p)}^{r_{\max}} \frac{w_j}{R_p} t(p, R_p) f(R_p) dR_p \quad (3)$$

where  $r_{\min}$  and  $r_{\max}$  are the minimal and maximal half-widths (or pore radii), respectively;  $w_j = 1$  for slitlike pores and 2 for cylindrical pores;  $r_k(p)$  is determined with modified Kelvin equation

$$r_k(p) = \frac{\sigma_s}{2} + t(p, R_p) + \frac{w_j \gamma v_m \cos \theta}{R_g T \ln(p_0/p)} \quad (4)$$

and  $t(p, R_p)$  can be computed with modified BET equation

$$t(p, R_p) = t_m \frac{cz}{(1-z)} \frac{[1 + (nb/2 - n/2)z^{n-1} - (nb+1)z^n + (nb/2 + n/2)z^{n+1}]}{[1 + (c-1)z + (cb/2 - c/2)z^n - (cb/2 + c/2)z^{n+1}]} \quad (5)$$

$t_m = a_m/S_{BET}$ ,  $b = \exp(\Delta\varepsilon/R_g T)$ ;  $\Delta\varepsilon$  is the excess of the evaporation heat due to the interference of the layering on the opposite wall of pores;  $t(p, R_p)$  is the statistical thickness of adsorbed layer;  $a_m$  is the BET monolayer capacity;  $c = c_s \exp((Q_p - Q_s)/R_g T)$ ;  $c_s$  is the BET coefficient

for adsorption on flat surface  $c_s = \gamma e^{\frac{E-Q_s}{R_s T}}$ ,  $Q_L$  is the liquefaction heat,  $E$  is the adsorption energy,  $\gamma$  is a constant;  $Q_s$  and  $Q_p$  are the adsorption heat on flat surface and in pores, respectively;  $z = p/p_0$ ;  $n$  is the number (noninteger) of statistical monolayers of adsorbate molecules and its maximal value for a given  $r_k$  is equal to  $(R_p - \sigma_s/2)/t_m$ ; and  $\sigma_s$  is the collision diameter of surface atoms. Typically, desorption data were utilized to compute the  $f(R_p)$  distributions with Eq. (3) and the regularization procedure [24] under non-negativity condition for  $f(R_p)$  with unfixed (automatically determined on the basis of F-test and confidence regions [24]) or fixed ( $\alpha = 0.01-0.001$ ) regularization parameter. The  $w$  value in Eqs. (3) and (4) is determined by the dependence of  $dV/dS$  on  $R_p$ , which, e.g., corresponds to  $R_p/2$  for cylindrical pores [8]. It should be noted that Eqs. (3)-(5) can be used not only for mesopores but also for micropores [27,28] in contrast to many of known adsorption isotherm equations, which can be used only for mesopores or only for micropores. For fumed oxides with spherical primary particles (or pyrocarbon with spherical particles), Eq. (4) should be replaced by following equation [8]

$$\ln \frac{p_0}{p} = \frac{\gamma w_m}{R_s T} \left[ \frac{1}{r} - \frac{2}{\sqrt{(R+t'+r)^2 - R^2} - r + R + t'} \right] \quad (6)$$

where  $R$  is the radius of primary particles, and  $t' = t + \sigma_s/2$ . The  $f(R_p)$  distributions determined with Eq. (3) and linked to the functions  $dV_p/dR_p$  can be easily transformed to the distributions  $f_s(R_p)$  with respect to  $dS/dR_p$  using the corresponding models of pores; e.g., for cylindrical pores

$$f_s(R_p) = \frac{2}{R_p} f_v(R_p) - \frac{2V_p}{R_p^2} \quad (7)$$

To compute  $f(E)$ , the modified deBoer-Hill-Toth (DHT) equation for mobile adsorption [10] for  $j$ -phase

$$\theta_j(p, E) = \frac{K_{DHT,j} p \exp(v_{DHT,j} \Theta - \frac{\Theta}{\chi_j - \Theta})}{1 + K_{DHT,j} p \exp(v_{DHT,j} \Theta - \frac{\Theta}{\chi_j - \Theta})} \quad (8)$$

where  $K_{DHT,j} = K_{DHT,j}^0(T) \exp(E/k_B T)$ ,  $K_{DHT}^0$ ,  $v_{DHT}$ , and  $\chi$  are constants;  $\Theta = a/a_m$  and  $p/p_0 < 0.1$ , was used as the kernel in Eq. (2). The values of  $K^0$ ,  $v$ , and  $\chi$  in Eq. (8) can be determined for individual materials using direct minimization methods with the starting magnitudes  $\chi = 1$  (corresponding to the deBoer-Hill (DH) equation),  $v_{DH} = 5.622$  and  $K_{DH}^0 = 7.31 \times 10^{-7}$  at 77.4K [10].

Additionally, the Fowler-Guggenheim (FG) equation (describing localized monolayer adsorption with lateral interaction)

$$\theta_l(p, E) = \frac{Kp \exp(zw\Theta/k_B T)}{1 + Kp \exp(zw\Theta/k_B T)} \quad (9)$$

(where  $K = K_0(T) \exp(E/k_B T)$  is the Langmuir constant for adsorption on monoenergetic sites and the pre-exponential factor  $K_0(T)$  is expressed in terms of the partition functions for an isolated gas and surface phases,  $z$  is the number of nearest neighbors of an adsorbate molecule (assuming  $z = 4$ ),  $w$  is the interaction energy between a pair of nearest neighbors,  $k_B$  is the Boltzmann constant,  $zw/k_B = 380K$  [29,30]) was used as a local isotherm  $\theta_l$ . A maximal

$p/p_0$  value for an isotherm portion used with Eq. (9) corresponded to coverage  $\Theta = a/a_m \approx 0.99$ .

(d)  $^1\text{H NMR}$ . The  $^1\text{H NMR}$  spectra were measured using a high-resolution WP-100 SY (Bruker) NMR spectrometer at 100 MHz working frequency and transmission band of 50 kHz. The temperature in the measuring chamber was adjusted with the accuracy of  $\pm 1\text{K}$  by means of a VT-1000 (Bruker) temperature controller. An electronic integrator registered the intensity of NMR signals with the accuracy of  $\pm 10\%$ . The  $^1\text{H NMR}$  chemical shifts for water adsorbed on carbosils from the gas phase (4-24 wt.%) or in the aqueous suspensions ( $\approx 6$  wt.% of solids) of adsorbents were determined with respect to tetramethylsilane (TMS) as an external standard. In order to prevent overcooling of the bulk water, the concentrations of unfrozen water were measured on suspension heating from 210K. This technique was described in details elsewhere [31-33].

## Results and discussion

Pyrocarbon grafted on the oxide surfaces by the pyrolysis of a variety of precursors reduces the total pore volume with  $C_C$  differently (Fig. 1). A maximal diminution of  $V_p$  is observed for Si-40 possessing mainly very narrow mesopores (Table 3,  $r_p$ ). For modified Si-60 with larger mesopores, this reduction is proportional to  $C_C$  and depends only slightly on the nature of organics (Fig. 1, Tables 1 and 2). A small decrease or even an increase in  $V_p$  is seen for fumed oxides after the cyclohexene pyrolysis (Fig. 1), as a porosity type of these oxides differs from that of mesoporous silica gel and corresponds to the gaps between spherical primary particles randomly packed in aggregates (whose apparent density is approximately 30% of the true density) [11,12,34]. At different  $C_C$  values, pyrocarbon produced by the carbonization of  $\text{C}_6\text{H}_{10}$  on fumed oxides provides a marked increase in the pore volume and the specific surface area (Table 5, Fig. 1); however, after  $\text{CH}_2\text{Cl}_2$  pyrolysis, reduction in  $V_p$  for C/A-300 is observed with  $C_C$ . The  $V_p$  values for fumed oxides are mainly linked to the channels in primary particle aggregates, but the empty space ( $V_{emp}$ ) in powders, which is connected with their apparent density ( $\rho_{ap}$ ) as follows  $V_{emp} \sim 1/\rho_{ap}$ , is significantly larger (e.g.,  $V_{emp} \approx 25 \text{ cm}^3/\text{g}$  for fumed silica A-300 at  $\rho_{ap} \approx 35\text{-}40 \text{ g/L}$ ) than  $V_p$  and linked to the structure of agglomerates and visible flocks. Notice that mechanochemical activation (MCA) of dry fumed silica powder in a ball-mill during 1-2 h enhance the effective pore volume ( $V_p \approx 1.10\text{-}1.14 \text{ cm}^3/\text{g}$  filled by nitrogen at  $p/p_0 \approx 0.99$ ) by approximately two times; however, MCA during 24 h reduces the effective pore volume to  $0.61 \text{ cm}^3/\text{g}$  close to  $V_p$  ( $0.67 \text{ cm}^3/\text{g}$ ) for initial silica powder [20]. For some carbosils ( $\text{AS}_3$  and CVD-titania/fumed silica  $\text{TS}_2$ ,  $\text{TS}_5$ ,  $\text{TS}_{17}$ ) at  $C_C = 17\text{-}28 \text{ wt.}\%$  (Fig. 1, Table 5), appearance of pyrocarbon deposits formed on the outer surfaces of aggregates of primary particles during pyrolysis of cyclohexene results in an enhancement of a portion of  $V_{emp}$  accessible for adsorbed nitrogen at  $p/p_0 \approx 0.99$  due to formation of tighter agglomerates similarly to those after MCA of silica powder. On the other hand, the pyrolysis of smaller molecule  $\text{C}_2\text{H}_2\text{Cl}_2$  can occur to a larger extent in channels of aggregates of primary particles of fumed silica that gives reduction of  $V_p$  dependent on  $C_C$  nearly linearly (Fig. 1). Additionally, the specific density of pyrocarbon is  $1.5\text{-}2 \text{ g/cm}^3$  [1], which is lower than that of fumed oxides (from  $\approx 2.2 \text{ g/cm}^3$  for silica to  $\approx 4.0 \text{ g/cm}^3$  for titania). Therefore relative loose pyrocarbon deposits formed by the cyclohexene pyrolysis (in contrast to other precursors carbonized on different oxide matrices (Fig. 1)) can enhance the effective porosity of C/fumed oxides (Table 5).

According to measurements of an accessible surface area of pyrocarbon prepared by the methylene chloride pyrolysis on Si-60 at 823K [7], the specific surface area of carbon deposits per se decreases from  $740 \text{ m}^2/\text{g}$  ( $C_C = 0.8 \text{ wt.}\%$ ) to  $56 \text{ m}^2/\text{g}$  ( $C_C = 35 \text{ wt.}\%$ ) but total

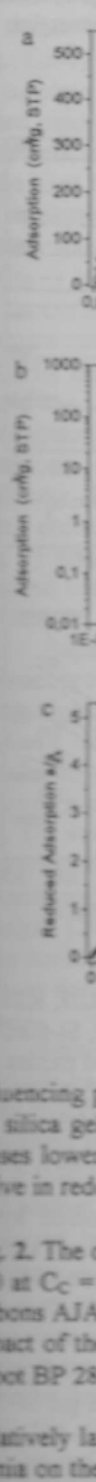
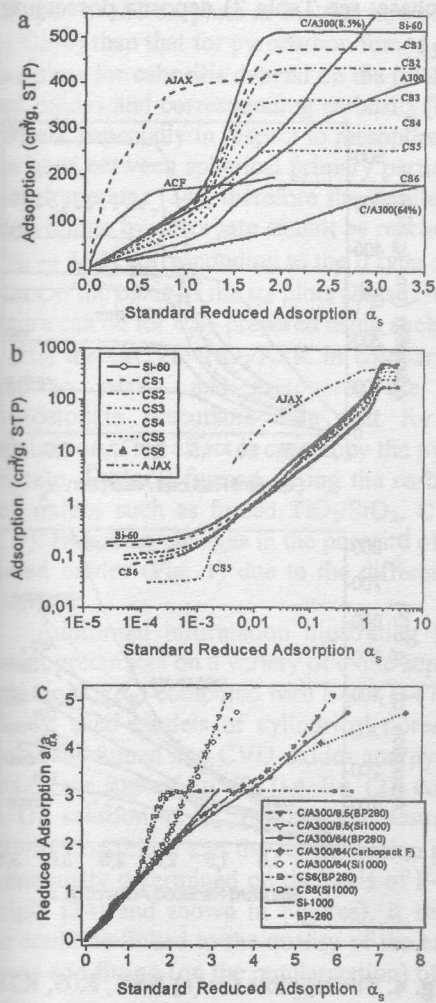


Fig. 2. The impact of carbon content  $C_C$  on the adsorption of nitrogen on Cabot BP 2000 silica. Relatively loose pyrocarbon deposits formed by the cyclohexene pyrolysis on the silica gel causes lower adsorption active in red.



influencing pyrolysis [2,5,16,17]. For instance, segregated and denser CVD-TiO<sub>2</sub> prepared on the silica gel surfaces at 873 K (K68 sample with rutile + anatase on silica gel KSK-2) [2] causes lower changes in  $S_{BET}$  and  $V_p$  than less dense titania (K28 with grafted anatase more active in redox reactions than rutile) prepared at a lower temperature (473K) (Table 4).

**Fig. 2.** The  $\alpha_s$  plots in (a) linear scale and (b) log-log scale for C/Si-60 (CS-*i*, Table 1), C/A-300 at  $C_C = 8.5$  (precursor C<sub>6</sub>H<sub>10</sub>) and 64 wt.% (CH<sub>2</sub>Cl<sub>2</sub>) (Table 5), highly porous activated carbons AJAX ( $S_{BET} = 1345$  m<sup>2</sup>/g) and ACF (579 m<sup>2</sup>/g) described in detail elsewhere [26]; (c) impact of the type of reference materials (silica gel Si-1000, carbon blacks Carbopack F and Cabot BP 280) on the  $\alpha_s$  plots for some carbosils.

Relatively larger changes in  $V_p$  and  $S_{BET}$  are observed after simultaneous CVD of carbon and titania on the pyrolysis of TiO(AcAc)<sub>2</sub> on Si-60 (Table 2). It should be noted that pyrolysis of

$S_{BET}$  decreases from 366 (CS-1) to 163 m<sup>2</sup>/g (CS-6), respectively. However, in the case of pyrocarbon-fumed silica (precursor CH<sub>2</sub>Cl<sub>2</sub>), diminution of  $S_{BET}$  (as well as  $V_p$ , Fig. 1) is smaller (Table 5) than those for pyrocarbon-silica gels (Tables 1-4). Typically, pyrocarbon formed on the silica surfaces (which do not have a marked catalytic activity in the pyrolysis) is composed of relatively large (especially at  $C_C > 10$  wt.%) and dense spherical particles [3-7] possessing low or negligible own internal (accessible) porosity [1]. In the case of mixed oxides [18,19] having a significant catalytic activity in the pyrolysis, carbon nuclei form near such active surface sites as Brønsted and Lewis acid sites catalyzing acid-base reactions or other sites (e.g., on anatase) active in redox reactions, whose distribution impacts such structural characteristics of pyrocarbon as its particle size distribution and aggregation features of tiny carbon particles (1-3 nm) to larger globules up to 200 nm observed in TEM micrographs [3,7,14,15]. Therefore changes in  $S_{BET}$  and  $V_p$  for C/Ts (Table 5, Fig. 1) are lower than those for C/fumed silica at close values of  $C_C$ ; i.e., pyrocarbon in C/Ts (cyclohexene carbonization) is more dispersed than that in C/fumed silica (CH<sub>2</sub>Cl<sub>2</sub> pyrolysis). For C/silica gel and C/CVD-TiO<sub>2</sub>/silica gel, these changes are larger due to the internal porosity of the silica gel matrix, crystalline and morphological features of CVD-titania

acetylacetonates of Ti, Cr, Co, Ni, Zn, and Zr on Si-60 results in formation of pyrocarbon-X (X is the corresponding oxide, silicate or metal phase, see Table 2) deposits possessing the morphology dependent on the nature of X [4].

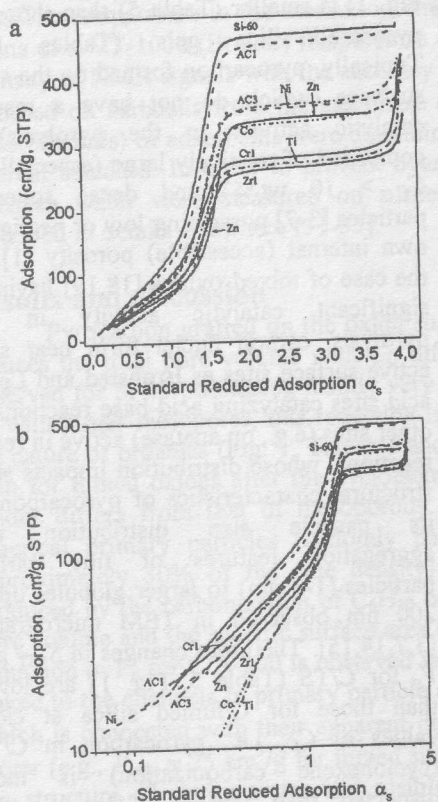


Fig. 3. The  $\alpha_s$  plots in (a) linear scale and (b) log-log scale for C/Si-60 (metal acetylacetonates and acetylacetone were precursors, Table 2).

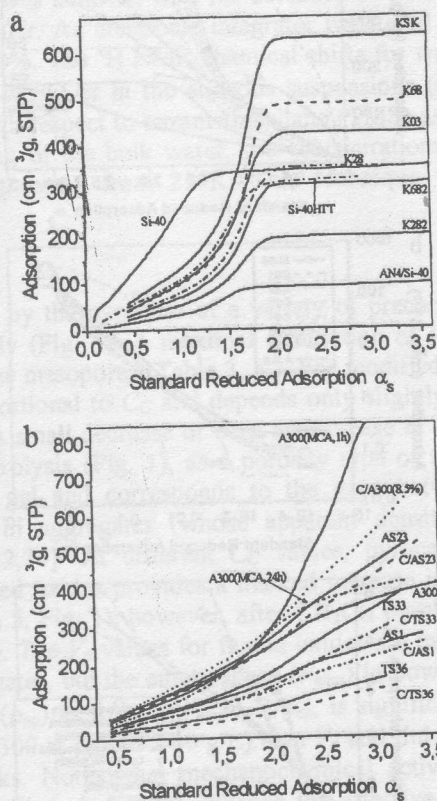


Fig. 4. The  $\alpha_s$  plots for (a) KSK, K03, K28, K282, K68, K682 (Table 4), Si-40, Si-40HTT, AN4/Si-40 (Table 3) and (b) fumed oxides and pyrocarbon/fumed oxides (Table 5). MCA-A300 (1 h or 24 h) is dry powder of fumed silica ball-milled for 1 or 24 h.

The values of  $V_p$ ,  $S_{BET}$ , and  $r_p$  decrease with  $C_C$  for the majority of the studied hybrid adsorbents (Tables 1-6) due to filling of mesopores by pyrocarbon (graphene clusters) and due to reduction of the empty volume between silica gel particles (diameter  $> 0.01$   $\mu\text{m}$ ) filled by carbon globules ( $10 < R_p < 200$  nm) grafted on the outer surfaces of these particles (resulting in the increase in the specific density of carbosils). The microporosity of CS-*i* samples as well as of other studied carbosils based on mesoporous silica gels is lower than that of pristine silica gel (whose microporosity is, however, insignificant), as their  $\alpha_s$  plots (silica gel Si-1000 and carbon blacks Carboxpack F (for AJAX and ACF) and Cabot BP 280 [35] were utilized as the reference adsorbents) differ significantly from those for such activated microporous

carbons as AJAX and ACF [27,28] (Figs. 2-4). Notice that the reference material type impacts the shapes of the  $\alpha_s$  plots at  $\alpha_s > 2$ ; however, this effect is weaker for pyrocarbon/silica gel (e.g., CS-6) than that for pyrocarbon/fumed silica (Fig. 2c). Besides, the relative differences in the  $\alpha_s$  plots for carbosils depend on the reference materials only slightly. The porosity type of fumed oxides and corresponding carbosils (Figs. 2a and 4b) differs considerably from that of silica gels, especially in respect to mesopores (as the empty volume in fumed oxides is linked to the gaps between spherical primary particles randomly but not dense packed in aggregates and agglomerates [34]; therefore the capillary effect in them is weak and total filling of the empty volume by adsorbate cannot be reached, as the plateau adsorption is not observed even at  $p/p_0 \rightarrow 1$  [3] corresponding to the II type of the isotherms [8,9]).

On the basis of the  $\alpha_s$  plots (Figs. 2-4), one can assume that larger changes in the pore structure can be for CS<sub>X</sub> prepared using such precursors as metal acetylacetonates (C/X/Si-60) or C<sub>6</sub>H<sub>10</sub> for C/CVD-TiO<sub>2</sub>/KSK in comparison with C/silica gels. Changes in the  $\alpha_s$  plots related to micro- and mesopores are greater for carbosils produced using metal acetylacetonate precursors than that for pure pyrocarbon prepared by acetylacetone carbonization. This effect is caused by the pyrolysis catalysis by a new X phase (oxide, metal, or silicate, Table 2) formed during the carbonization. A similar effect is observed for other mixed oxides such as fumed TiO<sub>2</sub>/SiO<sub>2</sub>, CVD-TiO<sub>2</sub>/fumed SiO<sub>2</sub>, CVD-TiO<sub>2</sub>/silica gel, etc. (Fig. 4). However, changes in the porosity of C/X/silica gels are typically larger than those for C/fumed oxides (Fig. 1) due to the differences in both the texture of matrices and formed pyrocarbon.

Additional information illustrating features of pyrocarbon deposits prepared using different precursors on a variety of oxide supports can be obtained on analysis of the pore size distributions  $f(R_p)$  computed with Eqs. (1)-(7) using the regularization procedure. To calculate  $f(R_p)$ , we used models of cylindrical pores for silica gel, pores (gaps) between spherical particles for fumed and CVD-oxides and pyrocarbon, and, at last, slitlike micropores at  $R_p < 2t_m$  using the sum of Eq. (3) (i.e. Eq. (2)) corresponding to each  $j$ -phase in hybrid adsorbents [22]. On solution of Eq. (3), one can assume that  $f(R_p) > 0$  over the total  $R_p$  range (non-negativity condition) and the regularization parameter  $\alpha$  can be fixed (0.01-0.001) or unfixed (automatically determined on the basis of F-test and confidence regions using the parsimony principle [24] and shown in Figures). It should be noted that the regularization parameter value could be linked to the quality of the experimental data, the nonuniformity of adsorbent surfaces and fitting (on the regularization) of a model adsorption isotherm to the experimental data.

Silica gel-pyrocarbon samples CS-*i* (Table 1) prepared by the pyrolysis of CH<sub>2</sub>Cl<sub>2</sub> on Si-60 can be considered as simple carbosils, as silica gel does not possess the catalytic ability in the pyrolysis and this precursor provides the simplest nuclei for carbon grains. The  $f(R_p)$  population at  $R_p < 1$  nm is negligibly low (Fig. 5) (utilized isotherm portions correspond to  $p/p_0 > 0.001$ ; but the use of lower pressures at  $p/p_0 > 10^{-8}$  leads to appearance of a narrow  $f(R_p)$  peak at  $R_p < 1$  nm), which corresponds to nearly pure mesoporous type of Si-60 and CS-*i* confirmed by their  $\alpha_s$  plot shapes with a very small deviations from the  $\alpha_s$  plots for the reference materials at  $\alpha_s < 1$ , as well as for other carbosils (Figs. 2-4). The main  $f(R_p)$  maximum shifts toward smaller  $R_p$  with increasing  $C_C$  due to partial filling of mesopores by pyrocarbon deposits (Fig. 5a). Own porosity of pyrocarbon particles is low and the  $f(R_p)$  intensity out of the PSD for pristine Si-60 (e.g., narrow peaks at  $R_p < 2$  nm for CS-1 and CS-5) can be linked to the gaps between tiny graphene particles and pore walls in mesopores of Si-60, the gaps between carbon particles per se or between the outer surfaces of silica gel particles and pyrocarbon deposits. Notice that the  $\alpha_s$  plot for CS-5 differs from others at low

adsorption (low  $p/p_0$ ) (Fig. 2b) and the  $f(R_p)$  peak at  $R_p \approx 1.1$  nm for CS-5 (Fig. 5) can be due to its structural feature. Also, the regularization parameter  $\alpha$  is the smallest (0.0028) for CS-5. Diminution of the fixed  $\alpha$  value to 0.01 for CS-6 gives a similar  $f(R_p)$  peak, especially with respect to  $f_S(R_p) = dS/dR_p$  (Fig. 5b). As the whole, the  $f_S(R_p)$  distributions possess greater intensity at smaller  $R_p$  in comparison with  $f_V(R_p)$  and the difference between them increases for large pores, e.g., in the case of hydrothermally treated silica gel (Fig. 5b, Si-60HTT).

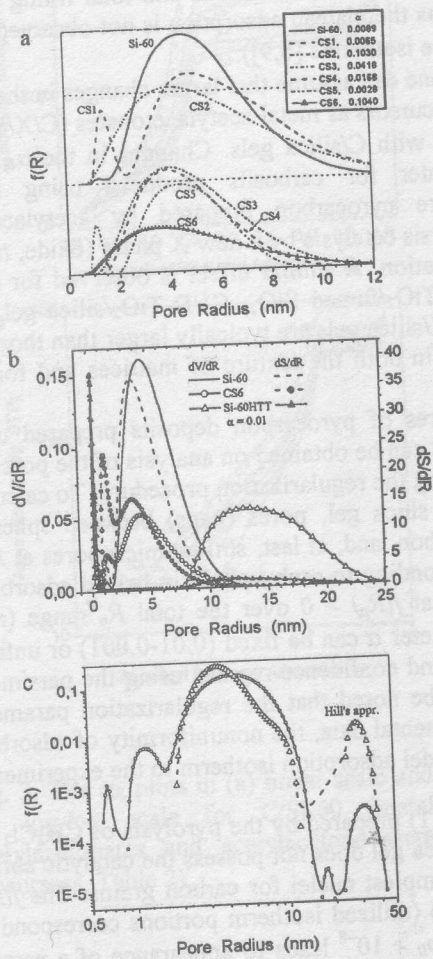


Fig. 5. Pore size distributions in respect to (a)  $dV_p/dR_p$  (unfixed regularization parameter  $\alpha$  shown in the figure legend) and (b)  $dS/dR_p$  or  $dV_p/dR_p$  for Si-60 and CS- $i$  samples ( $\alpha = 0.01$ ) (Table 1). Model of cylindrical pores for silica gel and pores between spherical particles for pyrocarbon; (c)  $f(R_p)$  computed using Hill's approximation and Eq. (4).

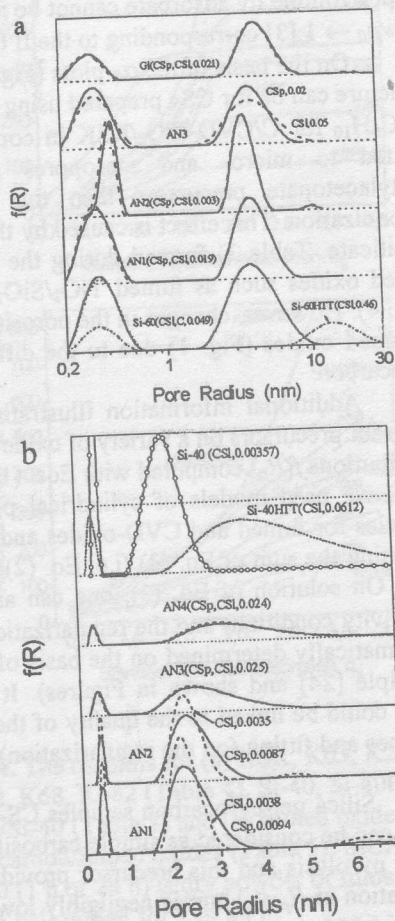


Fig. 6. Pore size distributions for (a) Si-60 and ANi/Si-60 and (b) Si-40 and ANi/Si-40 computed with unfixed  $\alpha$  value (shown in Figure) using models of cylindrical pores for silica gel and pores between spherical particles for pyrocarbon (labeled CSp, solid lines) or cylindrical pores for silica gel and slitlike pores for carbon (CSi, dashed lines).

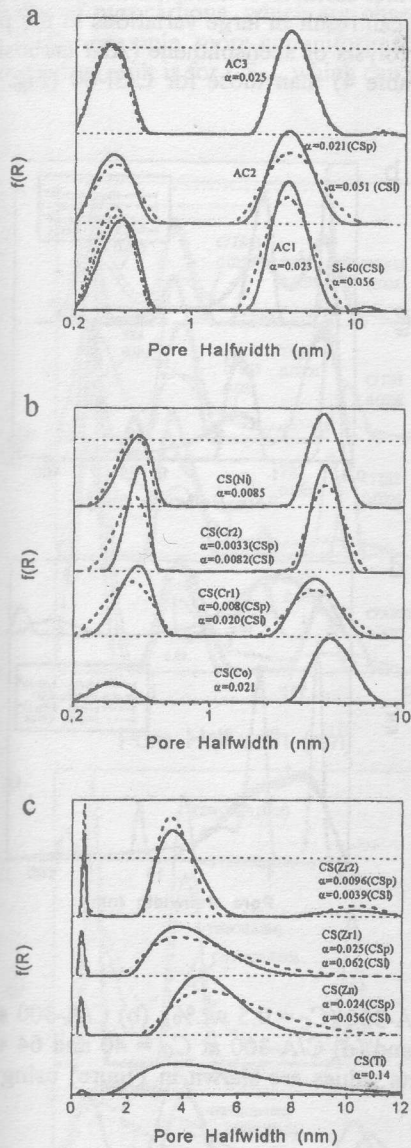


Fig. 7. Pore size distributions for (a) ACi, and (b, c) C/X/Si-60 computed with with unfixed  $\alpha$  value (shown in Figure) using models of cylindrical pores for silica gel and pores between spherical particles for pyrocarbon (labeled CSp, solid lines) or cylindrical pores for silica gel and slitlike pores (at  $R_p < 2t_m$ ) for carbon (CSI, dashed lines).

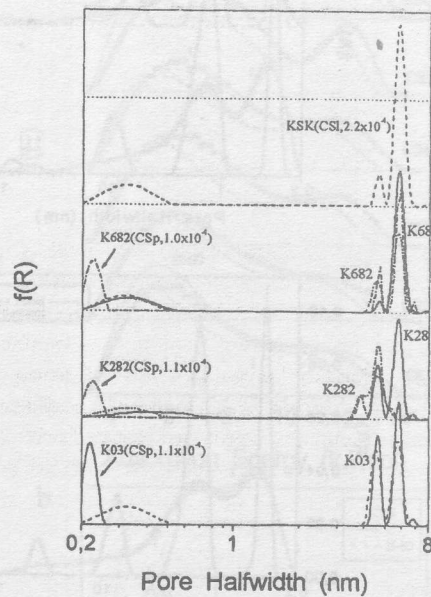


Fig. 8. Pore size distributions for KSK, K03, K28, K68, K282, and K682 (unfixed  $\alpha$  shown in Figure); two models (CSp and CSI) were used for hybrid adsorbents and the CSI model (slitlike pores at  $R_p < 2t_m$ ) was utilized for oxides.

Thus, according to previously published results [3,6,7] and these investigations, pyrocarbon formed on the pyrolysis of  $\text{CH}_2\text{Cl}_2$  on silica surfaces represents relatively dense and

practically nonporous particles from small graphene clusters (1-5 nm) in mesopores at  $R_p < 10$  nm up to globules of 100-200 nm grafted onto the outer surfaces of silica particles. Changes in the nature of the precursors or the oxide matrices can result in large variations in the pore structure of carbosils (Figs. 6-10). In the case of pyrolysis of acenaphthene (ANi carbosils), textural changes are larger for C/Si-40 (Fig. 6b, Table 4) than those for C/Si-60 (Fig. 6a,

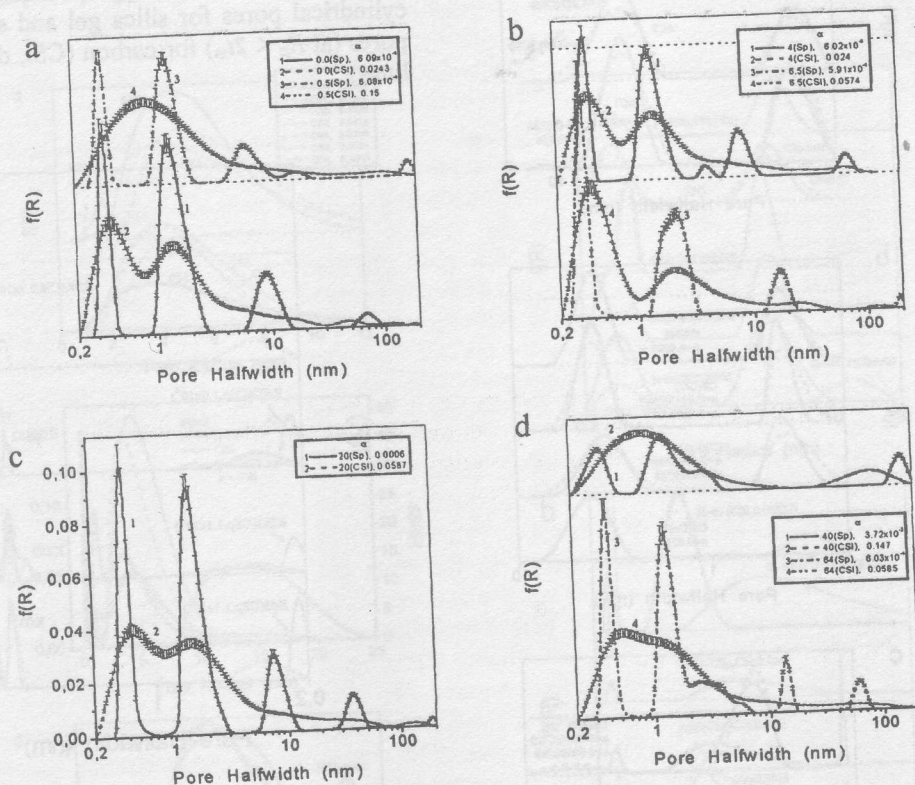
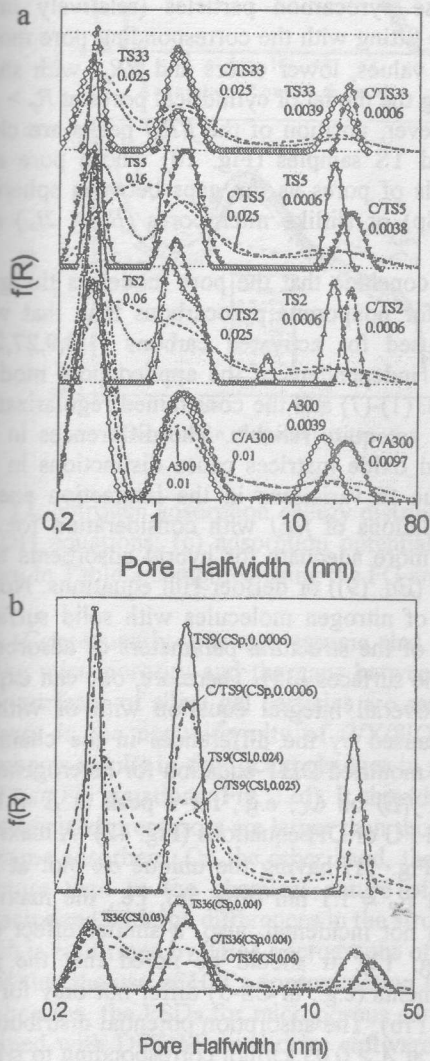


Fig. 9. Pore size distributions for (a) A-300 and C/A-300 ( $C_c = 0.5$  wt.%), (b) C/A-300 at  $C_c = 4$  and 6.5 wt.%, (c) C/A-300 at  $C_c = 20$  wt.%, and (d) C/A-300 at  $C_c = 40$  and 64 wt.% computed with unfixed regularization parameter (its values are shown in Figure) using two models of pores (CSp and CSI).

Tables 2 and 3). Acenaphthene  $C_{10}H_{12}$  does not have oxygen atoms in the molecules; however, its carbonization impact on Si-40 is akin to that observed on hydrothermal treatment of Si-40 at 423K (Fig. 6b). For C/Si-60, a similar effect is observed only on the glucose pyrolysis (Fig. 6a, G1). At the same time, changes in the pore structure of C/Si-60 due to the pyrolysis of acenaphthene (Fig. 6a) are analogous to those observed after the  $CH_2Cl_2$  carbonization (Fig. 5). However, larger textural changes in CS are observed after the pyrolysis of metal acetylacetonates (Fig. 7) due to the impact of a new X phase on the pyrolysis of subsequent portions of  $M(AcAc)_n$  (Tables 2 and 3) and the availability of oxygen atoms in the

molecules. Nevertheless, even for last precursor, the main effects are related to filling of silica gel mesopores by pyrocarbon and X phases (Figs. 7 and 8), despite the differences in the structure of pyrocarbons, which are observed in the TEM microphotographs of CS samples [3,4,7]. For example, more nonuniform and denser carbon deposits are observed for CS<sub>Ti</sub> and the opposite result is for CS<sub>Zn</sub>, which can be caused by the difference not only in the catalytic



**Fig. 10.** Pore size distributions for (a) A-300, C/A-300 ( $C_c = 8.5$  wt.%) CVD-TS, and C/CVD-TS, and (b) fumed TS and C/fumed TS ( $C_6H_{10}$  precursor) computed with unfixed regularization parameter (its values are shown in Figure) using two models of pores (CSp and CSi).

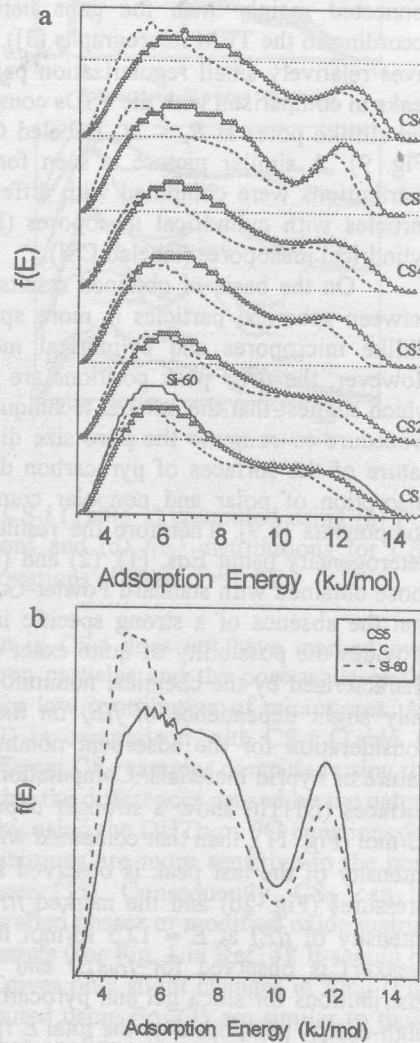


**Fig. 11.** Nitrogen adsorption energy distributions for (a) CS-*i* (Table 1) computed using DHTH (symbols and solid lines) and DHT (dashed lines) equations with fixed  $\alpha = 0.01$ ; and (b)  $f(E)$  for silica gel and pyrocarbon in CS5 computed with DHTH.

impact of the X phase on the pyrolysis but also in features of pyrocarbon distributions. Notice that Zn forms the silicate phase, but pyrolysis of  $\text{TiO}(\text{AcAc})_2$  results in formation of anatase crystallites of  $\sim 11$  nm [4]. Cobalt exists in  $\text{CS}_{\text{Co}}$  as a metallic phase (crystallite size 20-25 nm); nickel in  $\text{CS}_{\text{Ni}}$  is in both metallic (crystallite size  $\sim 25$  nm) and oxide phases ( $\sim 13$  nm); and  $\text{CS}_{\text{Zr-2}}$  includes zirconium dioxide ( $\sim 4$  nm) [4]. These various X particles can affect the pyrocarbon structure in C/X/Si-60 differently.

For C/fumed silica prepared by the pyrolysis of  $\text{CH}_2\text{Cl}_2$ , own porosity of pyrocarbon is connected mainly with the gaps between dense pyrocarbon particles (relatively large according to the TEM micrographs [3]). Therefore fitting with the corresponding pore model gives relatively small regularization parameter  $\alpha$  values, lower errors and  $f(R_p)$  with sharp peaks in comparison with the PSDs computed using the model of cylindrical pores at  $R_p > 2t_m$  and slitlike pores at  $R_p < 2t_m$  (labeled CSI). However, position of the  $f(R_p)$  peaks are close (Fig. 9). A similar picture is seen for C/TS and TS samples (Fig. 10) whose pore size distributions were computed with different models of pores as the gaps between spherical particles with cylindrical mesopores (labeled CSp) or slitlike micropores ( $R_p < 2t_m$ ) and cylindrical mesopores (labeled CSI).

On the basis of obtained results, one can conclude that the pore model as the gaps between spherical particles is more appropriate for nonporous pyrocarbons than that with slitlike micropores and cylindrical mesopores used for activated carbons [1,8,9,27,28]. However, the  $f(R_p)$  peak positions are practically independent of the applied pore models, which suggest that the utilized technique with Eqs. (1)-(7) and the constrained regularization procedure to compute the pore size distributions are quite reliable. The differences in the nature of the surfaces of pyrocarbon deposits and oxide matrices cause distinctions in the adsorption of polar and nonpolar compounds due to variations in the interaction energy components [8,9]. Therefore the results of calculations of  $f(E)$  with consideration for the heterogeneity using Eqs. (1), (2) and (8) can be more adequate for hybrid adsorbents than those obtained with standard Fowler-Guggenheim (Eq. (9)) or deBoer-Hill equations. Notice that the absence of a strong specific interaction of nitrogen molecules with solid surfaces provides the possibility of quite exact evaluation of the structural parameters of adsorbents characterized by the chemical nonuniformity of the surfaces [35]. Therefore, one can expect only slight dependence of  $f(E)$  on the type of overall integral equation with or without consideration for the adsorbent nonuniformity caused by the differences in the chemical nature of hybrid materials. Computations with the modified DHT equation for heterogeneous surfaces (DHTh) show a stronger dependence of  $f(E)$  on  $C_c$ , e.g., for a peak at  $E \approx 12.5$  kJ/mol (Fig. 11), than that computed with standard FG or DH equations (Fig. 12). A maximal intensity of the last peak is observed for CS-5 (Fig. 11) having the unique  $\alpha_s$  plot at low pressures (Fig. 2b) and the marked  $f(R_p)$  peak at  $R_p \approx 1.1$  nm (Fig. 5a); i.e., the maximal intensity of  $f(E)$  at  $E \approx 12.5$  kJ/mol for CS-5 is not incidental; also, a similar effect (but weaker) is observed for  $f_{\text{DH}}(E)$  and  $f_{\text{FG}}(E)$  (Fig. 12). It should be noted that the  $f(E)$  distributions for silica gel and pyrocarbon components (e.g., in CS-5) differ not only for the high-energy peak but over the total  $E$  range (Fig. 11b). The adsorption potential distributions for CS-*i* samples (Fig. 12c) depend on  $C_c$  slightly at  $A > 0.05$  kJ/mol corresponding to  $p/p_0 < 0.925$ . A  $f(A)$  minimum at this  $A$  value is linked to completion of secondary filling of mesopores corresponding to the main  $f(R_p)$  peak (Fig. 5). The inflection of  $f(A)$  curves at  $A$  between 1 and 4 kJ/mol corresponds to the availability of a small portion of micropores seen in  $f(R_p)$  in the case of the utilization of a low- pressure portions of the isotherms on the PSD computation. Microporous carbon AJAX has three minima at  $A > 0.9$  kJ/mol as it possesses bimodal micropore distribution [27,28] and its  $f(A)$  differs strongly from that for CS-*i* (Fig.

Fig. 12. Nitro  
(b) DH equa  
shown in Tab  
  
(12c) Conseq  
slitlike micro  
outer surface  
increase in th  
adsorbents  
DHTh or FG  
of carbonized  
the same ads  
structure tha  
characterized  
which is conf  
noted that the  
5c), besides,  
obtained with  
technique to  
(2) to comput  
for analysis o

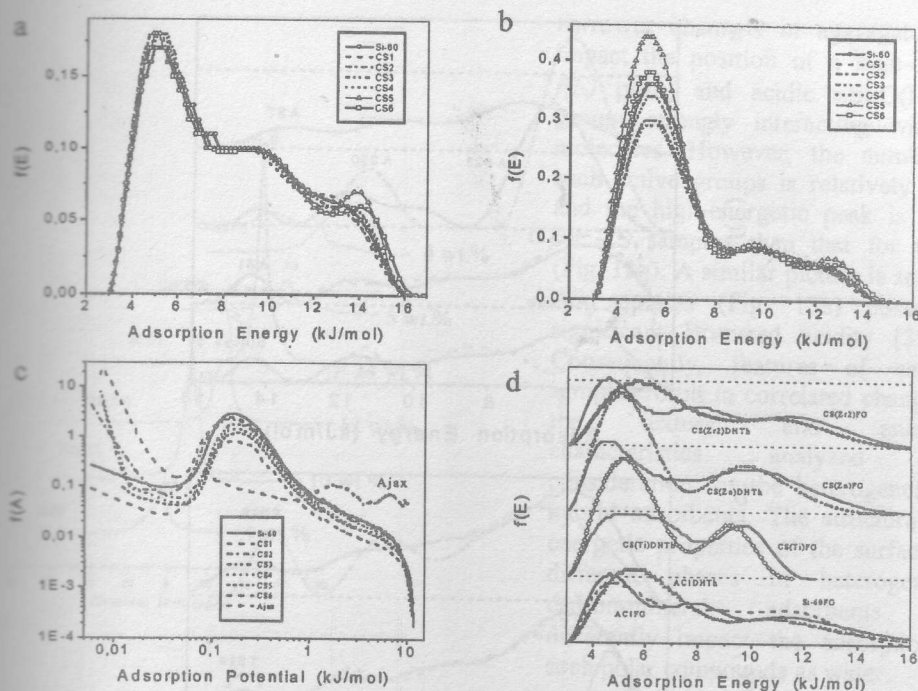


Fig. 12. Nitrogen adsorption energy distributions for CS-*i* (Table 1) computed using (a) FG; (b) DH equations; (c) adsorption potential distributions and (d)  $f(E)$  distributions for CS<sub>x</sub> shown in Table 2 computed using the FG and DHTh equations at fixed  $\alpha = 0.01$ .

(2c). Consequently, one can assume that pyrocarbon in CS-*i* does not have marked own slitlike microporosity and the gaps between pyrocarbon particles and the pore walls or the outer surfaces of silica gel particles are responsible for low contribution of micropores. An increase in the nonuniformity of C/X/SiO<sub>2</sub> (Table 2) in comparison with CS-*i* (Table 1) adsorbents results in significant changes in  $f(E)$  for different CS<sub>x</sub> samples computed using the DHTh or FG equations (Fig. 12d). It should be noted that the differences caused by the nature of carbonized precursors are larger than those caused by using the DHTh or FG equations for the same adsorbent. On the other hand, the  $f(E)$  distributions are more sensitive to the pore structure than to the chemical nature of the surfaces [35]. Consequently, CS<sub>x</sub> can be characterized by large differences in the structures of grafted phases or modified oxide matrix, which is confirmed by TEM micrographs of these materials (see Fig. 1 in Ref. 4). It should be noted that the use of Hill's approximation for Eq. (4) gives only slight changes in  $f(R_p)$  (Fig. 5c); besides, the PSDs for microporous carbons computed using Eq. (3) are similar to those obtained with DFT Micromeritics software [27,28] that confirms the reliability of the used technique to calculate the  $f(x)$  distributions. Utilization of the DHTh Eq. (8) and Eqs. (1) and (2) to compute  $f(E)$  for fumed oxides allows one to obtain detailed pictures (Fig. 13) fruitful for analysis of correlations between the structural (Figs. 1, 4b, 10) and energetic (Fig. 13)

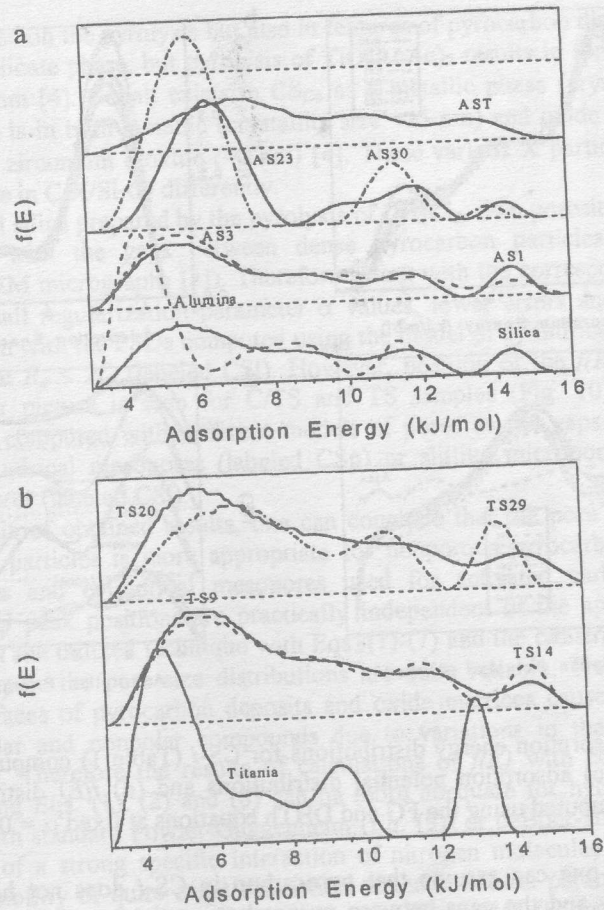


Fig. 13. Nitrogen adsorption energy distributions for fumed oxides (a) silica, alumina, AS and (b) titania and TS (Table 5) computed using DHTH (solid lines) and DHT (dashed lines) equations with fixed  $\alpha = 0.001$ .

characteristics. For instance, titania has relatively low  $S_{BET}$  (large primary particles with the average diameter of 25 nm) and a small  $V_p$  (Table 5); however, titania as a semiconductor possesses a relatively narrow energetic gap ( $\sim 3.8$  eV) and large polarizability, which cause significant dispersion interaction with adsorbed nonpolar nitrogen molecules. Therefore titania has a large  $f(E)$  peak at 13 kJ/mol, however, shifted toward smaller  $E$  in comparison with that for fumed titania-silica possessing larger  $S_{BET}$  (smaller primary particles and

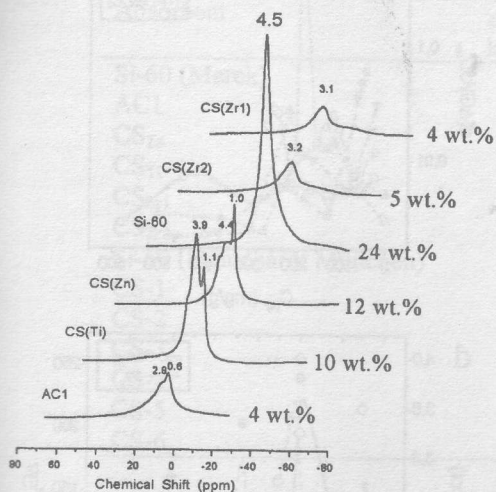


Fig. 14. Chemical shifts (in respect to TMS) for  $^1\text{H}$  NMR spectra of water adsorbed on Si-60, AC1 and C/X/Si-60 (Table 2) at room temperature (adsorbed water concentration is shown in Figure).

This heterogeneity could be analyzed using the  $^1\text{H}$  NMR method with freezing-out of the bulk water [31-33]. The application of this method to water adsorbed on the most complex carbosils  $\text{CS}_x$  prepared by the pyrolysis of metal acetylacetonates, as well as for CS-i at different  $C_C$  values [6], shows substantial differences in the  $^1\text{H}$  NMR spectra recorded at room temperature (Fig. 14), amounts of unfrozen water ( $C_{uw}$ ) and changes in the Gibbs free energy  $\Delta G$  of the interfacial water at T between 210 and 273 K depending on the nature of grafted deposits and their concentrations (Fig. 15, Table 6). In Table 6,  $\Delta G_{max}$  corresponds to changes in the Gibbs free energy of the first monolayer of the interfacial water strongly bound to the adsorbent surfaces;  $\Delta G_{\Sigma}$  (in  $\text{mJ per m}^2$  of the adsorbent surface) is the overall changes in  $G$  due to the water interaction with the surfaces distorting the interfacial water unfrozen at  $T < 273$  K, and  $C_{uw}^{max}$  denotes the total amounts of unfrozen water at  $T \rightarrow 273$  K [31-33]. In the case of mesoporous silica gel Si-60 (Merck), the  $\Delta G(C_{uw})$  function is nearly linear (Fig. 15a); i.e., the amounts of the unfrozen water decreases nearly linearly with lowering temperature. Notice that  $\Delta G(C_{uw})$  for Si-60 (Merck) differs from that for Si-60 (Schuchardt München) (Figs. 15a and 15c), and the PSDs for these initial silica gels differ (Figs. 5-7). For carbosils,  $\Delta G(C_{uw})$  has a complex shape due to the heterogeneity of the surfaces. A portion of the  $\Delta G(C_{uw})$  curves with a maximal incline (Figs. 15a and 15c) and large derivatives (Fig. 15b) corresponds to the boundary between strongly and weakly bound

narrower channels in aggregates can impact the position of a high-energy  $f(E)$  peak) and acidic  $\equiv\text{Si-O(H)-Ti}\equiv$  groups strongly interacting with  $\text{N}_2$  molecules. However, the number of such active groups is relatively small and the high-energetic peak is lower for TS samples than that for titania (Fig. 13b). A similar picture is seen for AS samples (Fig. 13a) possessing significant Brønsted acidity [32,33]. Consequently, features of carbosil samples result in correlated changes in the textural and energetic characteristics analyzed with consideration for the heterogeneity of hybrid adsorbents. The structural and energetic properties of the surfaces of different phases in heterogeneous carbon-mineral adsorbents can differently impact the adsorption of such polar compounds as water.

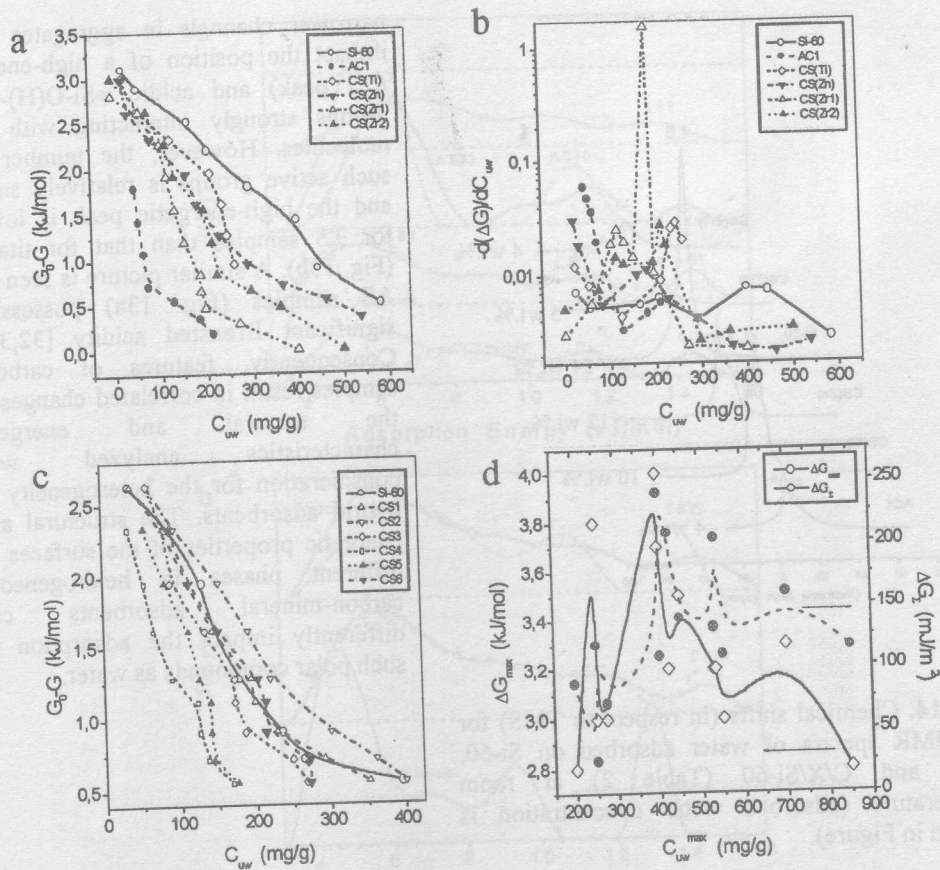


Fig. 15. Changes (a) and (c) in the Gibbs free energy ( $\Delta G$ ) and (b) its derivative  $-d(\Delta G)/dC_{uw}$  for the interfacial water in the frozen aqueous suspensions (210-273 K) of (a, b) Si-60 (Merck), AC1 and C/X/Si-60 (Table 2); and (c) Si-60 (Schuchardt München) and CS-*i* (Table 1) estimated from the <sup>1</sup>H NMR spectra; (d) relationships between the total amounts of unfrozen water at  $T \rightarrow 273$ K ( $C_{uw}^{max}$ ) and changes in the Gibbs free energy of the first monolayer  $\Delta G_{max}$  and overall  $\Delta G_{\Sigma}$  values for CS<sub>X</sub> and CS-*i* samples.

waters, as small changes in  $C_{uw}$  result in large variations in  $\Delta G$ . One can assume that this effect is also connected with a water layer interacting with different phases (oxide and pyrocarbon) with various Gibbs free energies but close temperatures of water freezing at  $T < 273$  K. In the case of pure pyrocarbon on silica gel surfaces (AC1), the  $\Delta G(C_{uw})$  plot lies to the left in comparison with those for CS<sub>X</sub> (Fig. 15a) due to weaker interaction between nonpolar or slightly polar pyrocarbon particles and interfacial water.

Among CS-*i* samples, the maximum of nonuniformity is observed for CS<sub>2</sub> and CS<sub>3</sub> samples (Fig. 15b). The relationships between  $\Delta G_{\Sigma}$  and  $C_{uw}^{max}$  values are not linear, which explains the nonuniformity of the samples.

#### Conclusions

On the basis of the structural and surface area data, with consideration of the pore size distribution, we are relatively confident that the data correspond to the pore structure, which c...

**Table 6**  
 Characteristics of the Interfacial Water Layers in the Frozen Aqueous Suspensions of Carbonsils

Adsorbent	$\Delta G_{max}$ , kJ/mol	$\Delta G_{\Sigma}$ , mJ/m <sup>2</sup>	$C_{uw}^{max}$ , mg/g
Si-60 (Merck)	3.3	160	700
AC1	3.8	26	250
CS <sub>Zn</sub>	3.2	204	535
CS <sub>Ti</sub>	3.2	208	424
CS <sub>Zr1</sub>	2.8	88	200
CS <sub>Zr2</sub>	3.0	118	250
Si-60 (Schuchardt München)	2.8	115	850
CS-1	3.0	110	550
CS-2	3.2	132	530
CS-3	4.0	109	400
CS-4	3.0	72	275
CS-5	3.5	139	450
CS-6	3.7	240	400

Among CS-*i* samples the most incline is observed for CS-5 (Fig. 15c), which also has a larger maximum of  $f(E)$  at  $E = 14$  kJ/mol (Fig. 12a). However, CS-2 can possess a maximal nonuniformity, as its  $\Delta G(C_{uw})$  plot lies to the right in comparison with those for other CS-*i* samples (Fig. 15c) in contrast to CS<sub>X</sub>, whose  $\Delta G(C_{uw})$  graphs shift toward lower  $C_{uw}$  in comparison with that for pristine Si-60 (Fig. 15a). The observed differences in  $\Delta G(C_{uw})$  for CS<sub>X</sub> and CS-*i* samples can be caused by deposit distribution features as the X phase can catalyze the pyrolysis depending on the nature of the X phase (Table 2). Therefore new portions of pyrocarbon are formed around the X grains. In the case of carbonization of such organics as CH<sub>2</sub>Cl<sub>2</sub>, C<sub>6</sub>H<sub>10</sub>, C<sub>12</sub>H<sub>10</sub>, carbon grains are more active as the reaction promoters than silica surfaces [2] that leads to enlargement of carbon particles, and relatively large particles up to 200 nm can be formed on the outer silica gel surfaces at  $C_C > 10$  wt.% [2-7]. Consequently, the silica patches in CS-*i* can be more easily accessible than those in CS<sub>X</sub>, which explains the observed differences in  $\Delta G(C_{uw})$  for these carbonsils (Fig. 15). The relationships between the total amounts of unfrozen water on CS<sub>X</sub> and CS-*i* at  $T \rightarrow 273$ K ( $C_{uw}^{max}$ ) and changes in the Gibbs free energy  $\Delta G_{max}$  of the first monolayer and overall  $\Delta G_{\Sigma}$  values are nonlinear (Fig. 15d) due to the influence of the nature of the surfaces, their nonuniformity, charge distribution and PSDs, etc.

### Conclusions

On the investigations of the structural and energetic characteristics of hybrid pyrocarbon-mineral adsorbents including texturally and chemically different phases, their structural and energetic features should be analyzed using the overall isotherm approximation with consideration for the adsorbent heterogeneity.

In the case of C/SiO<sub>2</sub>, the pyrocarbon deposits represent mainly dense globules, which are relatively large and possess low porosity, as changes in the pore size distributions correspond to reduction of mesopores of the supports practically without appearance of new pores, which can be assigned to the carbon phase per se.

Structural features of titania-silicas prepared using silica gel and fumed silica matrices and different techniques cause alterations in the distribution of pyrocarbon on the supports, the particle size distribution and other properties of deposits and adsorbents as the whole. In general, pyrocarbon at the concentration from several to dozens percents consists mainly of large individual dense globules and possesses low own porosity provided mainly by the gaps between outer surfaces of the matrices and pyrocarbon globules. Tiny dense graphene particles (clusters) can fill mesopores of the supports or gaps (channels) between particles of oxides. Pyrocarbon forms preferably near the titania particles (CVD-TiO<sub>2</sub>) or TiO<sub>2</sub>/SiO<sub>2</sub> (as well as Al<sub>2</sub>O<sub>3</sub>/SiO<sub>2</sub>) interfaces possessing catalytic activity in the pyrolysis. Pyrocarbon formation results in dramatic changes in the porosity of titania-silica gel during simultaneous CVD processes for both pyrocarbon and titania phases on the TiO(AcAc)<sub>2</sub> pyrolysis. Similar but smaller effects are observed for C/X/Si-60 prepared by the pyrolysis of Zn and Zr acetylacetonates or for C/CVD-TiO<sub>2</sub>/KSK. Thus, the choice of oxide matrices, organic precursors and techniques for the synthesis of oxides and carbon deposits allow one to change substantially the structural characteristics of hybrid carbon-mineral adsorbents in desirable direction.

### Acknowledgements

This research was supported by NATO (grant No. EST.CLG.976890), the Polish State Committee for Scientific Research and Ministry of High Education and Science of Ukraine (grant No. 2M/303-99).

### References

1. Felonov V.B. Porous Carbon. Nauka, Novosibirsk, 1995. 513 p.
2. CVD-Titania/Silica Gel Carbonized due to Pyrolysis of Cyclohexene / V.M. Gun'ko, R. Leboda, W. Grzegorzczak, J. Skubiszewska-Zieba, M. Marciniak, A.A. Malygin, A.A. Malkov // *Langmuir*. - 2000. - 16, N 7. - P. 3227-3243.
3. Fumed Silica Carbonized Due to Pyrolysis of Methylene Chloride. / V.M. Gun'ko, J. Skubiszewska-Zieba, R. Leboda, V.I. Zarko // *Langmuir*. - 2000. - V. 16, No 2. - P. 374-382.
4. Silica Gel Modified Due to Pyrolysis of Acetylacetone or Metal (Ti, Cr, Co, Ni, Zn, Zr) Acetylacetonates / V.M. Gun'ko, R. Leboda, J. Skubiszewska-Zieba, J. Rynkowski // *J. Colloid Interface Sci.* - 2000. - 231, N 1. - P. 13-25.
5. Structural and Energetic Nonuniformities of Pyrocarbon-Mineral Adsorbents / V.M. Gun'ko, R. Leboda, V.V. Turov, F. Villieras, J. Skubiszewska-Zieba, S. Chodorowski, M. Marciniak // *J. Colloid Interface Sci.*, submitted.
6. Characterization of Spatial and Energetic Structures of Carbon-Silica Gels / V.M. Gun'ko, R. Leboda, B. Charmas, F. Villieras // *Colloid. Surf. A.* - 2000. - V. 173, N 1-3. - P. 159-169.
7. High Resolution Argon and Nitrogen Adsorption Assessment of the Surface Heterogeneity of Carbosils / F. Villieras, R. Leboda, B. Charmas, F. Bardot, G. Gerard, W. Rudzinski // *Carbon*. - 1998. - V. 36, N 10. - P. 1501-1510.
8. Gregg S.J., Sing K.S.W. Adsorption, Surface Area and Porosity. Moscow: Mir, 1970. - 407 p.
9. Adamson A.W. Physical Chemistry of Surface. Moscow: Mir, 1979. 568 p.
10. Toth J. Uniform Interpretation of Gas/Solid Adsorption. // *Adv. Colloid Interface Sci.* - 1995. - V. 55, P. 1-240.
11. Legrand A.P., Ed. The Surface Properties of Silicas. New York: Wiley, 1998. 470 p.

12. Gun'ko V.M. Impact of the nature and the state of highly disperse oxides on their adsorptive properties // *Teoret. Eksperim. Khim.* 36, N 1, 1-29 (2000).
13. Characterization of CVD-Titania/Silica Gel by Means of Low Pressure Nitrogen Adsorption / V.M. Gun'ko, F. Villieras, R. Leboda, M. Marciniak, B. Charmas, J. Skubiszewska-Zięba // *J. Colloid Interface Sci.* – 2000. – V. 230, N 2. – P. 320-327.
14. Structure of Silica Gel Si-60 and Pyrocarbon/Silica Gel Adsorbents Thermally and Hydrothermally Treated / V.M. Gun'ko, R. Leboda, J. Skubiszewska-Zięba, V.V. Turov, P. Kowalczyk // *Langmuir*, in press.
15. Gun'ko V.M., Leboda R., Skubiszewska-Zięba J. Impact of Thermal and Hydrothermal Treatments on Structural Characteristics of Silica Gel (Si-40) and Pyrocarbon/Silica Gel Adsorbents // *Colloids Surf. A*, submitted.
16. Structure of CVD-Titania/Silica Gel / R. Leboda, V.M. Gun'ko, M. Marciniak, A.A. Malygin, A.A. Malkov, W. Grzegorzczak, B.J. Trznadel, E.M.Pakhlov, E.F.Voronin // *J. Colloid Interface Sci.* – 1999. – P. 23-39.
17. Structure of Carbonized Mesoporous Silica Gel/ CVD-Titania / R. Leboda, M. Marciniak, V.M. Gun'ko, W. Grzegorzczak, A.A. Malygin, A.A. Malkov // *Colloids Surf. A.* – 2000. – V. 167, N 3. – P. 275-285.
18. Fumed oxides modified due to pyrolysis of cyclohexene / V.M. Gun'ko, R. Leboda, V.I. Zarko, M. Marciniak, J. Skubiszewska-Zięba, W. Grzegorzczak, E.M. Pakhlov, E.F. Voronin, E. Chibowski // *Colloids Surf. A*, submitted.
19. Highly Dispersed X/SiO<sub>2</sub> and C/X/SiO<sub>2</sub> (X = Alumina, Titania, Alumina/Titania) in the Gas and Liquid Media / V.M. Gun'ko, V.I. Zarko, R. Leboda, M. Marciniak, W. Janusz, S. Chibowski // *J. Colloid Interface Sci.* – 2000. – V. 230. – P. 396-409.
20. Connections between structural properties and treatments of fumed silicas / V.M. Gun'ko, E.F. Voronin, I. F. Mironyuk, R. Leboda, J. Skubiszewska-Zięba, E.M. Pakhlov, N.V. Guzenko, A.A. Chuiko // *Colloids Surf. A.*, submitted.
21. Surface Properties of Mesoporous Carbon-Silica Gel Adsorbents / R. Leboda, V.V. Turov, B. Charmas, J. Skubiszewska-Zięba, V.M. Gun'ko // *J. Colloid Interface Sci.* – V. 2000. – V. 223, N 1. – P. 112-125.
22. Gun'ko V.M. Consideration for adsorbent complexity on analysis of their structural and energetic parameters // *Teoret. Eksperim. Khim.* – 2000. – 36, N 6. – C. 349-353.
23. Szombathely M.v., Brauer P., Jaroniec M. The Solution of Adsorption Integral Equations by Means of the Regularization Method // *J. Comput. Chem.* – 1992. V. 13, N 1. – P. 17-32.
24. Provencher S.W. A Constrained Regularization Method for Inverting Data Represented by Linear Algebraic or Integral Equations. *Comp. Phys. Comm.* – 1982. - V. 27. – P. 213-227.
25. Gun'ko V.M., Voronin E.F., Zarko V.I., Pakhlov E.M. // *CVD-Germania on Pyrogenic Silica* // *Langmuir.* – 1997. – V. 13, N2. – P. 250-259.
26. CVD-Titania on Fumed Silica Substrate / V.M. Gun'ko, V.I. Zarko, V.V. Turov, R. Leboda, E. Chibowski, L. Holysz, E.M. Pakhlov, E.F. Voronin, V.V. Dudnik, Yu.I. Gornikov // *J. Colloid. Interface Sci.* – 1998. – V. 198. – P. 141-156.
27. Nguyen C., Do D.D. A New Method for the Characterization of Porous Materials. // *Langmuir.* – 1999. – V. 15. - P. 3608-3615.
28. Gun'ko V.M., Do D.D. Characterization of Pore Structure of Carbon Adsorbents Using Regularization Procedure. *Colloids Surf. A*, in press.
29. Choma J., Jaroniec M. Energetic and Structural Heterogeneity of Synthetic Microporous Carbons // *Langmuir.* –1997. V. 13, N 5. – P. 1026-1030.
30. Jaroniec C.P., Gilpin R.K., Jaroniec M. Adsorption and Thermogravimetric Studies of Silica-Based Amide Bonded Phases // *J. Phys. Chem. B.* – 1997. – V. 101, N 35. – P. 6861-6866.

31. Gun'ko V.M., Turov V.V. Structure of Hydrogen Bonds and  $^1\text{H}$  NMR Spectra of Water at the Interface of Oxides // *Langmuir*. – 1999. – V. 15, N 19. – P. 6405-6415.
32. Active Site Nature of Pyrogenic Alumina/Silica and Water Bound to Surfaces / V.M. Gun'ko, V.V. Turov, V.I. Zarko, E.F. Voronin, V.A. Tischenko, V.V. Dudnik, E.M. Pakhlov, A.A. Chuiko // *Langmuir*. – 1997. – V. 13, N6. – P. 1529-1544.
33. Characterization of Fumed Alumina/Silica/Titania in the Gas Phase and Aqueous Suspension / V.M. Gun'ko, V.I. Zarko, V.V. Turov, R. Leboda, E. Chibowski, E.M. Pakhlov, E.V. Goncharuk, M. Marciniak, E.F. Voronin, A.A. Chuiko // *J. Colloid. Interface Sci.* – 1999. – V. 220, N2. – P. 302-323.
34. Basic Characteristics of Aerosil. Technical Bulletin Pigments. No 11, Hanau: Degussa AG, 1997. 81 p.
35. (a) Kruk M., Li Z., Jaroniec M., Betz W.R. Nitrogen Adsorption Study of Surface Properties of Graphitized Carbon Blacks // *Langmuir*. – 1999. – V. 15, N 4. – P. 1435-1441; (b) Kruk M., Jaroniec M., Gadkaree K.P. Nitrogen Adsorption Studies of Novel Synthetic Active Carbons // *J. Colloid Interface Sci.* – 1997. – V. 192. – P. 250-256; (c) Jaroniec M., Kruk M., Olivier J.P. Standard Nitrogen Adsorption Data for Characterization of Nanoporous Silicas // *Langmuir*. – 1999. – V. 15, N 16. – P. 5410-5413.

Abstract

Mes  
quaternary  
titanium(IV  
presence H  
mol. %we  
diffraction  
pore volum  
synthesized  
type and bi  
prepared de

Introduct

Rem  
mesostructu  
aluminosilic  
diameter fr  
the use of  
carriers due  
[4-5]. Cons  
contained in  
preparation  
conditions o  
800 °C and  
materials in  
inclusion of  
new materia  
with cataly  
adsorption s  
types is in  
SIS must  
materials  
reaction of  
reaction of  
containing s